Applied Physics Letters

Contribution of multiple plasmon scattering in low-angle electron diffraction investigated by energy-filtered atomically resolved 4D-STEM

Cite as: Appl. Phys. Lett. **121**, 213502 (2022); https://doi.org/10.1063/5.0129692
Submitted: 06 October 2022 • Accepted: 05 November 2022 • Published Online: 21 November 2022

H. L. Robert, B. Diederichs and K. Müller-Caspary

Applied Physics Letters ARTICLE scitation.org/journal/apl

Contribution of multiple plasmon scattering in low-angle electron diffraction investigated by energy-filtered atomically resolved 4D-STEM

Cite as: Appl. Phys. Lett. **121**, 213502 (2022); doi: 10.1063/5.0129692
Submitted: 6 October 2022 · Accepted: 5 November 2022 ·
Published Online: 21 November 2022

H. L. Robert,[1,2] B. Diederichs,[3,4] and K. Müller-Caspary[1,3,a)]

AFFILIATIONS

[1]Ernst Ruska-Centre for Microscopy and Spectroscopy with Electrons (ER-C), Forschungszentrum Jülich, Wilhelm-Johnen-Strasse, 52428 Jülich, Germany
[2]2nd Institute of Physics, RWTH Aachen University, Templergraben 55, 52062 Aachen, Germany
[3]Department of Chemistry, Ludwig-Maximilians-Universität München, Butenandtstrasse 5-13, 81377 Munich, Germany
[4]Institute of Biological and Medical Imaging, Helmholtz Zentrum München, 85764 Neuherberg, Germany

[a)]Author to whom correspondence should be addressed: k.mueller-caspary@cup.lmu.de

ABSTRACT

We report the influence of multiple plasmon losses on the dynamical diffraction of high-energy electrons, in a scanning transmission electron microscopy (STEM) study. Using an experimental setup enabling energy-filtered momentum-resolved STEM, it is shown that the successive excitation of up to five plasmons within the imaged material results in a subsequent and significant redistribution of low-angle intensity in diffraction space. An empirical approach, based on the convolution with a Lorentzian kernel, is shown to reliably model this redistribution in dependence of the energy-loss. Our study demonstrates that both the significant impact of inelastic scattering in low-angle diffraction at elevated specimen thickness and a rather straightforward model can be applied to mimic multiple plasmon scattering, which otherwise is currently not within reach for multislice simulations due to computational complexity.

Due to its excellent spatial resolution and the inherent capability of multidimensional characterization, scanning transmission electron microscopy (STEM) is a key technique for the precise characterization of materials down to atomic resolution. In particular, quantitative STEM approaches based on multislice simulations,[1,2] including thermal diffuse scattering,[3,4] enabled the measurement of thickness, strain, and chemical composition[5–7] by comparison of the experimental high-angle scattering with composition- and thickness-dependent simulations. Furthermore, the introduction of ultrafast cameras[8–12] provided access to the detailed distribution of intensity in momentum space, containing both high- and low-angle scattering. Consequently, the momentum-resolved STEM (MR-STEM) technique evolved to be a promising candidate for the comprehensive characterization of nanostructures by exploiting the details of diffraction patterns recorded in dependence of the probe position, over a wide range of scattering angles.

Nevertheless, early work[13] revealed a dramatic mismatch between state-of-the-art quasi-elastic simulations and experiments at scattering angles below 50 mrad. Subsequent studies[14,15] elucidated the relevance of inelastic scattering, in particular, due to plasmon excitations. Specifically, single plasmon scattering involves the application of a transition potential to the elastic wave function at a variety of positions in the volume of the specimen, the elastic propagation of all emerging waves down to the specimen exit face separately, and their incoherent summation.[14] It follows that multiple plasmonic excitations could be included through the application of the same scheme in a nested manner. Nevertheless, due to the resulting computational complexity, simulations are currently usually limited to the single plasmon excitation case. Consequently, quantifying the effect of multiple plasmon scattering on the intensity distribution at low scattering angles both experimentally and conceptually suggests itself as a prerequisite for employing the wealth of low-angle information to augment quantitative material characterization.

In this work, a dedicated MR-STEM setup in an aberration-corrected Hitachi HF 5000 microscope operated with an acceleration voltage $U = 200$ kV is used to record diffraction patterns in dependence of scan position and energy-loss, at atomic spatial resolution.

To this end, an ultrafast Medipix Merlin4EM camera[9] was mounted behind an energy-filtering and imaging device (CEFID, CEOS Ltd.).[16] A scan pixel size of 22 pm and a dwell time of 1 ms per scan position were used, while the semi-convergence angle was set to 20 mrad, leading to a Rayleigh resolution of approximately 76 pm. A TEM lamella of bulk Al prepared by focused ion beam milling was imaged in the [100] zone axis in two different regions, denoted by A and B in the following. The local thicknesses were determined using the log-ratio approach.[17,18] Here, the division of the unfiltered by the elastic signal yielded ratios of 1.74 and 14.68 for regions A and B, respectively. Using an inelastic mean free path of $\Lambda = 134$ nm,[19] this results in local specimen thicknesses of (A) 74 and (B) 360 nm. An example electron energy-loss (EEL) spectrum taken close to region B is shown in Fig. 1, where the first five plasmon peaks are clearly visible at multiples of approximately $E = 15.3$ eV energy-loss corresponding to a single plasmon excitation. Several MR-STEM datasets were recorded with 10 eV-wide energy windows centered on the zero-loss peak (ZLP) and on the individual plasmon peaks PL 1 to PL 5. It is noteworthy that the energy range of 10 eV per window was chosen to ensure that each recording would contain only electrons associated with the respective plasmonic peak.

The effect of energy-loss on the scattered intensity is first studied via position-averaged convergent beam electron diffraction (PACBED) patterns obtained in regions A and B, for each energy-loss separately. In the plasmon-loss case, this is justified because the excitation is delocalized in real-space. In order to visualize the effect in a compact manner, the angular dependence was calculated by averaging the PACBED intensities azimuthally as well, as shown in Fig. 2(a) for dataset A. Electron-optics-related elliptical distortions at the level of the detector were accounted for by an anisotropic coordinate frame for the scattering angles.[20,21] Note that the azimuthal integration forms the basis for angle-resolved STEM (AR-STEM), which initially revealed the importance of inelastic scattering employing annular detectors.[13,22] By convention, the data are normalized to the incident intensity I_0 and to the solid angle.

It is instructive to analyze the angular intensity distribution in dependence of increasing energy-loss, as presented in Fig. 2(a). Within the Ronchigram below 20 mrad, the intensity remains almost constant and is separated from the dark field via a step-like drop. This step is sharpest for elastically scattered electrons contained in the ZLP and consecutively smears out with an increasing number of excited plasmons. In particular, the Ronchigram border is barely visible in the log-scale plot after five plasmon excitations. The ratios of the angular scattering of subsequent plasmon excitations are plotted in Fig. 2(b). This explicitly shows that each energy-loss obeys its own angular behavior, such that multiple plasmon scattering can have a significant impact in AR-STEM if the specimen thickness is large enough to yield significant intensity in the respective plasmon peaks.

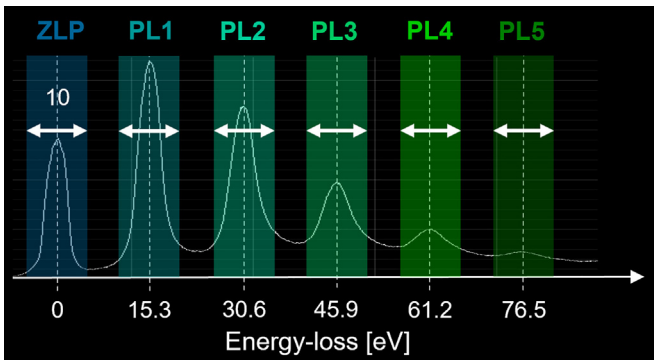

FIG. 1. Energy-loss spectrum of an Al specimen with a thickness of approximately 360 nm. The zero-loss peak corresponds to elastically scattered electrons, while electrons detected in the plasmon-loss peaks PL 1-5 have excited 1-5 plasmons while passing through the specimen. The energy windows at which MR-STEM data were recorded are indicated as well.

Also in 2D, the PACBED patterns in Fig. 2(c) obtained for the different energy-losses suffer from a strong blurring of sharp features present in the elastic ZLP data, which is amplified at each energy-loss. Finally, the loss-dependent bright field (BF) STEM images in Fig. 2(d) are obtained by summing all detected electrons within the primary beam. Although decreasing, elastic contrast and atomic resolution are preserved in real-space[23,24] with an increasing number of plasmon excitations. Indeed, the co-occurrence of elastic and inelastic scattering ensures that, within an electron wave having lost energy at a certain point of its propagation through the specimen, interference of the Bragg beams still occurs in the far-field. In the present study, the atomic-resolution BF data confirms the stability of instrument and specimen throughout the recordings making up the five-dimensional dataset.

The results obtained in the approximately five times thicker region B are given in Fig. 3. Qualitatively, the same arguments hold as to the loss-dependent subsequent angular broadening. It should be noted that inelastic scattering involving one to four plasmon excitations exceeds the elastically scattered number of electrons, as seen in Fig. 3(a). Whereas such elevated thicknesses are beyond common STEM applications, on the one hand, they are still used in quantitative convergent-beam electron diffraction; on the other hand, where the alleviation of inelastic scattering effects is often required.[25] Here, the thicknesses of 74 and 360 nm, respectively, serve as common and extreme cases to check the reliability of the empirical description of the momentum transfer associated with plasmon-losses, as presented in the following.

In that respect, it is relevant to recall the implication of the angle-dependent ratios in Figs. 2 and 3(b). If inelastic scattering had not changed the angular dependence of the scattered intensity, the ratio would be constant, that is, solely the energy of the electrons would change without any momentum transfer. For single inelastic scattering, earlier work[14,22,26] utilized the convolution of simulated diffraction patterns with a kernel derived from a transition potential as an approximation to an explicit inelastic simulation including dynamical scattering. This approximation consists of assuming commutativity of propagation and transition potential for inelastic scattering within the multislice model.[14] Here, a Lorentzian kernel $L_1(q)$ according to the dipole approximation[27] is used as follows:

$$L_1(q) = p_1\left(\frac{L_0}{q^2 + q_E^2}\right), \tag{1}$$

where p_1 represents the probability to excite a plasmon, L_0 is a normalization factor and q_E is a spatial frequency characteristic for the energy-loss. In the present case, a theoretical value $q_E \approx 0.0153$ nm^{-1} can be obtained from[27]

$$q_E = \frac{1}{\lambda}\sin\left(\frac{E}{2eU}\right), \tag{2}$$

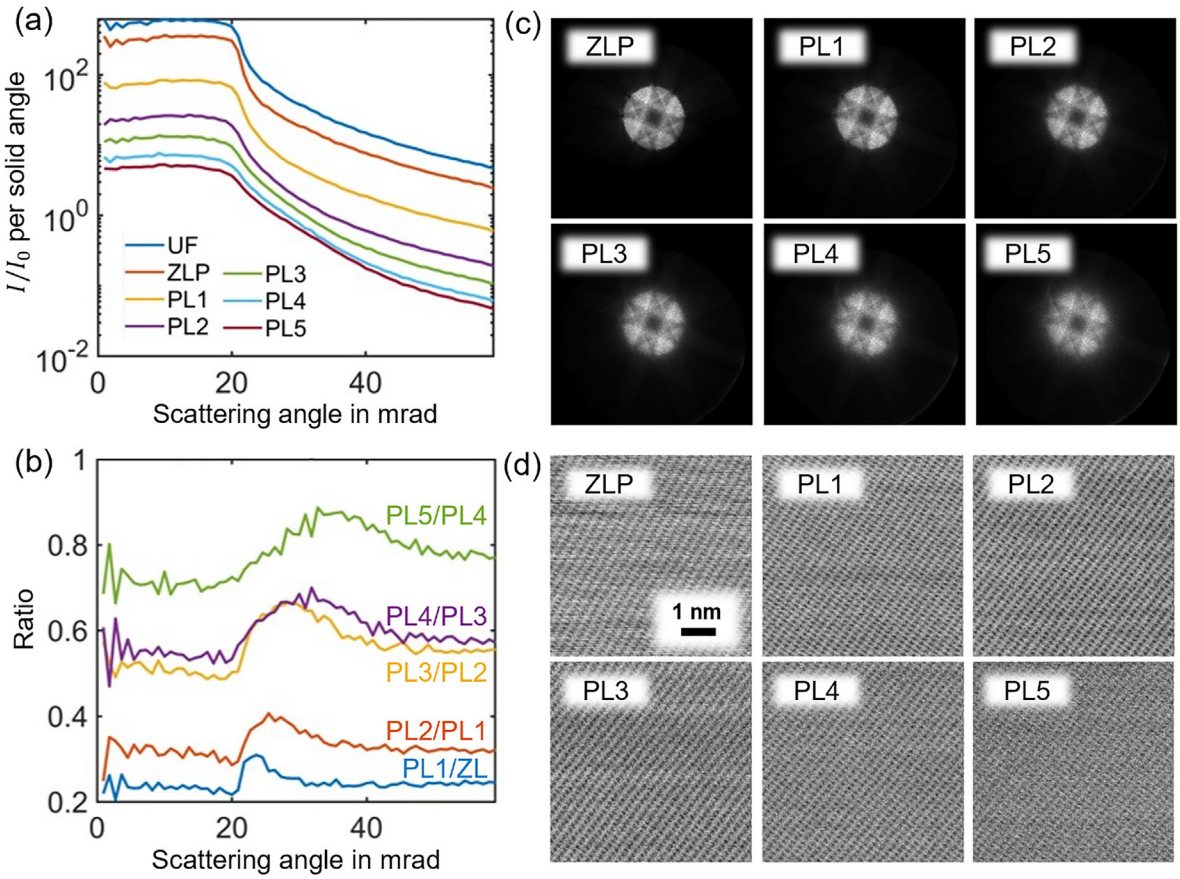

FIG. 2. Results of the energy-filtered MR-STEM experiments performed in region A with a thickness of 74 nm. (a) Position- and azimuthally averaged angular dependences of scattered intensity, per Sr, and normalized to I_0, for the unfiltered (UF) case, zero-loss-peak (ZLP) and up to five plasmon excitations (PL 1-5). (b) Angle-dependent ratio of successive inelastic intensities from (a). (c) PACBED patterns. (d) BF images.

with λ being the electron wavelength and e being the elementary charge. The dipole approximation is typically valid up to angles between 10 and 20 mrad, where L_1 is cut off.[28] Assuming that the diffraction pattern for a single plasmon-loss can be derived from a quasi-elastic simulation $I_{\mathrm{FP}}(\vec{q})$ employing the frozen phonon multislice approach, it is given by

$$I_{\mathrm{PL}}^{(1)}(\vec{q}) = I_{\mathrm{FP}}(\vec{q}) \otimes L_1(q), \tag{3}$$

and the zero-loss pattern is obtained by

$$I_{\mathrm{ZL}}(\vec{q}) = (1 - p_1) \cdot I_{\mathrm{FP}}(\vec{q}), \tag{4}$$

being the original simulation with the first plasmon-loss intensity removed. To account for multiple plasmon scattering and obtain $I_{\mathrm{PL}}^{(n)}(\vec{q})$, Eq. (3) must be applied recursively by convolving $I_{\mathrm{PL}}^{(n-1)}(\vec{q})$ with a kernel $L_{(n)}(\vec{q})$. It is reasonable to assume $L_{(n)}(\vec{q}) = L_1(q)$ since each plasmon scattering event obeys the same underlying physics. By using the Fourier convolution theorem, the dependence of scattered intensity after n plasmon-losses is straightforwardly obtained from a simulation $I_{\mathrm{FP}}(\vec{q})$ via

$$I_{\mathrm{PL}}^{(n)}(\vec{q}) = \mathcal{F}^{-1}\left[\mathcal{F}[I_{\mathrm{FP}}(\vec{q})](\vec{r}) \left(\tilde{L}_1(r)\right)^n\right](\vec{q}), \tag{5}$$

with $\tilde{L}_1(r)$ being the Fourier transform of $L_1(q)$. This indicates a decay of the plasmon scattering according to p_1^n, for which $p_1 = 1 - e^{-\frac{t}{\Lambda_P}}$ has proven applicable with Λ_P being the mean free path for plasmon scattering and t being the specimen thickness. For bulk Al, a value of $\Lambda_P = 160$ nm can be employed,[19] leading to $p_1 \approx 0.37$ for region A and $p_1 \approx 0.89$ for region B.

Multiple plasmon scattering is dominant in region B, which makes it a suitable example to study to which extent a quasi-elastic frozen phonon multislice PACBED simulation for 360 nm-thick Al [100], in combination with Eq. (5), can represent the experimentally observed angular broadening. The black curve in Fig. 4(a) represents the radial intensity per solid angle of the native simulation I_{FP}, of which only 11% remain in the elastic signal (ZLP) shown in blue. Scattered intensities calculated for up to five subsequent plasmon excitations with $q_E = 0.015\,\mathrm{nm}^{-1}$ (corresponding to 5 pixels in the simulation) are depicted too. They show an exponential decay of intensity with the number of plasmons according to p_1^n. Furthermore, a strong angular broadening affects the Ronchigram edge at 20 mrad. By summing up the elastic (ZLP) signal and all plasmon-losses, the red curve

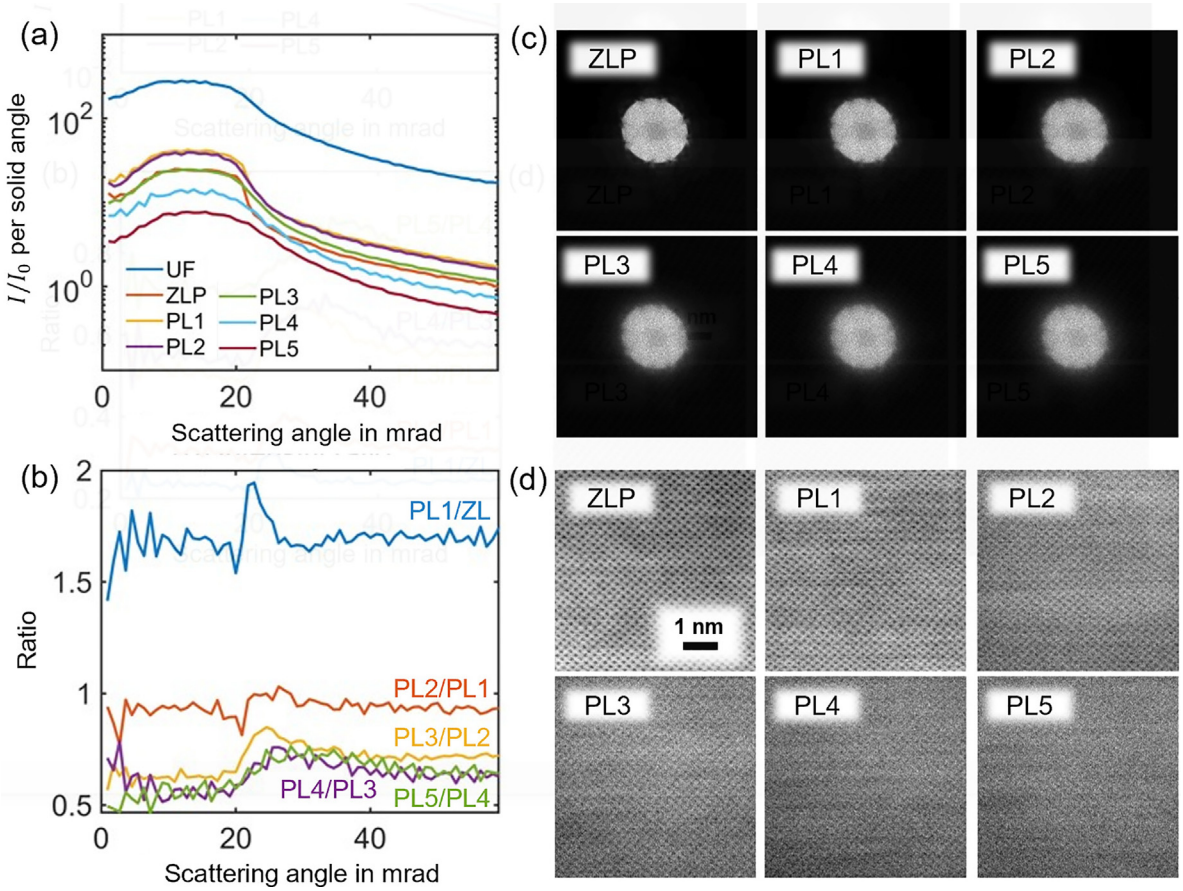

FIG. 3. Results of the energy-filtered MR-STEM experiments performed in region B with a thickness of 360 nm. (a) Position- and azimuthally averaged angular dependences of scattered intensity, per Sr, and normalized to I_0, for the unfiltered (UF) case, zero-loss-peak (ZLP) and up to five plasmon excitations (PL 1-5). (b) Angle-dependent ratio of successive inelastic intensities from (a). (c) PACBED patterns. (d) BF images.

is obtained, which can be interpreted as the simulated unfiltered (UF) angular dependence. Note that both features and magnitudes of the simulations based on the convolutional approach fit the experimental counterpart in Fig. 3(a) rather well. Differences in the scaling of the individual plasmon contributions are expected due to the small width of the energy windows which do not include the respective plasmon peaks completely.

The dependence of the plasmon-loss-induced angular broadening on specimen thickness suggests an analysis of the number of excitations that need to be considered at a given thickness, which is presented in Fig. 4(b). For thicknesses between 90 and 360 nm, the angular dependencies have been calculated as in Fig. 4(a), however, by taking only $0, \ldots, 4$ plasmon-losses into account to calculate the unfiltered result. Then, the difference ΔI to a simulation $I^{(5)}$, including five plasmon excitations, was calculated. For the material and thickness range dealt with here, this can be regarded as converged owing to Fig. 1. Figure 4(b) depicts the relative error $\Delta I/I^{(5)}$ in dependence of scattering angle, specimen thickness, and number of losses included.

Whereas the neglect of plasmon excitations leads to errors of up to 50% in all cases, taking only the broadening due to a single excitation into account is already sufficient for 90 nm thick specimens. For a thickness of 180 nm, the error becomes low if two plasmon-losses are considered. At even higher thicknesses, including three excitations appears sufficient. Of course, these conclusions depend on the characteristic spatial frequency q_E and the mean free path Λ_P. However, the former does not vary strongly among a wide range of materials, such that the thicknesses in terms of Λ_P in Fig. 4(b) should provide a rather general guide for the number of plasmons to consider in an AR-STEM experiment.

Furthermore, the experimental results presented in Figs. 2 and 3 can be exploited directly in an empirical verification of the applicability of a Lorentzian function to represent the redistribution of intensity due to inelastic scattering. Since the PACBED patterns corresponding to individual energy windows can be identified as the $I_{PL}^{(n)}$ intensities, according to the model given here, they could be used to perform a fitting of the $L_{(1)}(q)$ function, by adjustment of a parametric q_E and minimization of the sum of squared difference.[29] It is noteworthy that, because of the loss of intensity due to the small width of the energy windows, it is not expected to obtain a perfect agreement in the value of p_1, excitation-wise. For this reason, the fitted Lorentzian was multiplied by a coefficient, itself being adjusted for each individual

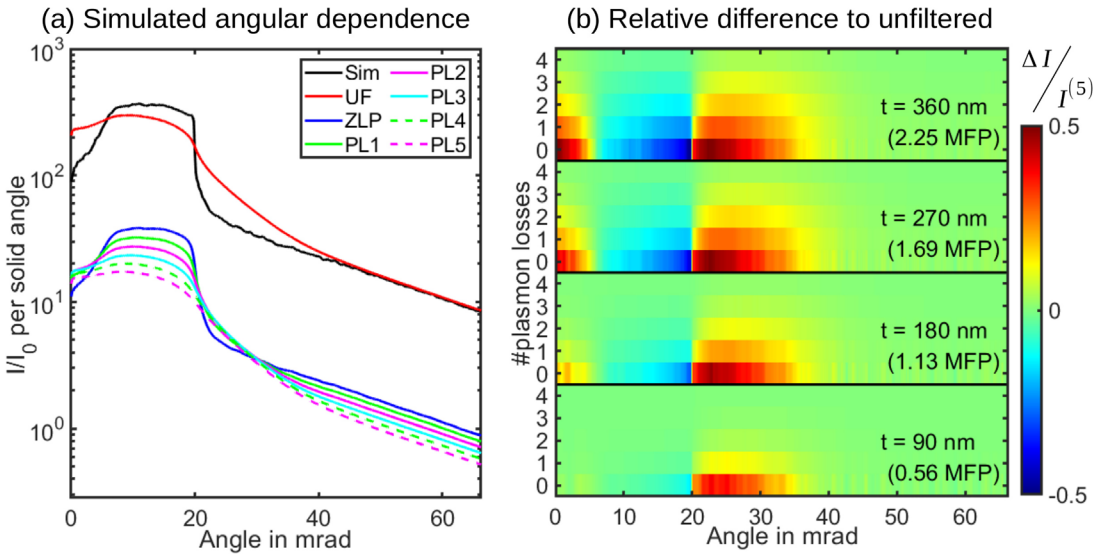

FIG. 4. (a) Simulated angular dependence for 360 nm specimen thickness in dependence of the energy-loss, based on a frozen phonon multislice result. Lorentzian parameters were $q_E = 0.015\,\mathrm{nm}^{-1}$ with a cutoff at 15 mrad. (b) Simulated relative error when 0–5 plasmons are included in dependence of scattering angle and specimen thickness. The case with 5 plasmon excitations included is considered as unfiltered.

transition. Although the convolution was performed using the two-dimensional diffraction patterns, the difference was obtained from the one-dimensional angular dependencies. The cutoff of the Lorentzian was set to 15 mrad.

Values extracted for q_E are $0.0221\,\mathrm{nm}^{-1}$ in region A and $0.0214\,\mathrm{nm}^{-1}$ in region B, the fit being concluded with an average relative error of (A) 3.92% and (B) 6.38%. Those experimentally determined characteristic scattering angles only lead to a marginal improvement of 0.5% of the fit as compared to the theoretical value of $0.0153\,\mathrm{nm}^{-1}$. The reason is the finite and rather large sampling of diffraction space by the pixels imposed as a constraint from the camera. With this shallow minimum in mind, one can conclude that the convolution-based model using the theoretical characteristic spatial frequency q_E represents the experiments rather well. It is also noteworthy that the quality of fit is generally higher for the region A data, which can be related to the higher intensity of the corresponding diffraction patterns. This is, in turn, due to the lower thickness traveled by the electrons within the material, ensuring that a smaller proportion of those are scattered beyond the camera range, mainly due to thermal diffuse scattering.

To conclude, we demonstrated the successive broadening of features in diffraction patterns of high-energy electrons due to the excitation of multiple plasmons. An experimental setup has been demonstrated to collect momentum- and energy-resolved STEM data efficiently and routinely using contemporary ultrafast cameras. The validity of a computationally efficient, empirical approach to account for the momentum transfer associated with multiple plasmon excitations has been demonstrated in experiment and extensive multislice frozen-phonon simulations. This finding suggests that, even if an inelastic scattering event occurs within a 3D volume and is hence followed by elastic dynamical scattering, the assumption of commutativity[14] in the multislice model remains reasonable when considering azimuthal intensity averages in diffraction patterns. As a consequence, the inherent computational complexity of accurately representing inelastic scattering could be alleviated by substituting the rigorous description, involving the propagation of mutually incoherent waves, with a series of convolution steps performed on a conventional simulation. With a significant improvement of the agreement of low-angle scattering in experiment and simulation in a straight-forward model to be applied after conventional quasi-elastic simulations, the quantitative evaluation of low-angle scattering becomes within reach. In particular, this addresses the evaluation of the local chemical composition of several constituents in a specimen simultaneously by exploiting their individual fingerprints at characteristic angles in an angle-resolved STEM setup.[13]

This work was supported by the Initiative and Network Fund of the Helmholtz Association (Germany) under Contract Nos. VH-NG-1317 and ZT-I-0025 and by the Deutsche Forschungsgemeinschaft under Grant No. EXC 2089/1-390776260.

AUTHOR DECLARATIONS

Conflict of Interest

The authors have no conflicts to disclose.

Author Contributions

Hoel Laurent Robert: Data curation (equal); Formal analysis (equal); Investigation (equal); Methodology (equal); Visualization (equal); Writing – original draft (equal). **Benedikt Diederichs:** Methodology (equal); Software (equal); Writing – review & editing (equal). **Knut Müller-Caspary:** Conceptualization (lead); Data curation (equal); Funding acquisition (lead); Methodology (lead); Project administration (lead); Resources (lead); Software (equal); Supervision (lead); Writing – review & editing (lead).

DATA AVAILABILITY

The data that support the findings of this study are available from the corresponding author upon reasonable request.

REFERENCES

[1]J. M. Cowley and A. F. Moodie, "The scattering of electrons by atoms and crystals. I. A new theoretical approach," Acta Crystallogr. **10**, 609–619 (1957).
[2]D. F. Lynch and M. A. O'Keefe, "n-Beam lattice images. II. Methods of calculation," Acta Crystallogr., Sect. A **28**, 536–548 (1972).
[3]J. M. LeBeau and S. Stemmer, "Experimental quantification of annular dark-field images in scanning transmission electron microscopy," Ultramicroscopy **108**, 1653–1658 (2008).
[4]A. Rosenauer, M. Schowalter, J. T. Titantah, and D. Lamoen, "An emission-potential multislice approximation to simulate thermal diffuse scattering in high-resolution transmission electron microscopy," Ultramicroscopy **108**, 1504–1513 (2008).
[5]A. Rosenauer, K. Gries, K. Müller, A. Pretorius, M. Schowalter, A. Avramescu, K. Engl, and S. Lutgen, "Measurement of specimen thickness and composition in Alx Ga1 - x N/GaN using high-angle annular dark field images," Ultramicroscopy **109**, 1171–1182 (2009).
[6]A. Rosenauer, T. Mehrtens, K. Müller, K. Gries, M. Schowalter, P. Venkata Satyam, S. Bley, C. Tessarek, D. Hommel, K. Sebald, M. Seyfried, J. Gutowski, A. Avramescu, K. Engl, S. Lutgen, P. V. Satyam, S. Bley, C. Tessarek, D. Hommel, K. Sebald, M. Seyfried, J. Gutowski, A. Avramescu, K. Engl, and S. Lutgen, "Composition mapping in InGaN by scanning transmission electron microscopy," Ultramicroscopy **111**, 1316–1327 (2011).
[7]T. Grieb, K. Müller, O. Rubel, R. Fritz, C. Gloistein, N. Neugebohrn, M. Schowalter, K. Volz, and A. Rosenauer, "Determination of the chemical composition of GaNAs using STEM HAADF imaging and STEM strain state analysis," Ultramicroscopy **117**, 15–23 (2012).
[8]K. Müller, H. Ryll, I. Ordavo, S. Ihle, L. Strüder, K. Volz, J. Zweck, H. Soltau, and A. Rosenauer, "Scanning transmission electron microscopy strain measurement from millisecond frames of a direct electron charge coupled device," Appl. Phys. Lett. **101**, 212110 (2012).
[9]R. Plackett, I. Horswell, E. N. Gimenez, J. Marchal, D. Omar, and N. Tartoni, "Merlin: A fast versatile readout system for Medipix3," J. Instrumentation **8**, C01038 (2013).
[10]K. Müller-Caspary, A. Oelsner, and P. Potapov, "Two-dimensional strain mapping in semiconductors by nano-beam electron diffraction employing a delay-line detector," Appl. Phys. Lett. **107**, 072110 (2015).
[11]H. Ryll, M. Simson, R. Hartmann, P. Holl, M. Huth, S. Ihle, Y. Kondo, P. Kotula, A. Liebel, K. Müller-Caspary, A. Rosenauer, R. Sagawa, J. Schmidt, H. Soltau, and L. Strüder, "A pnCCD-based, fast direct single electron imaging camera for TEM and STEM," J. Instrum. **11**, P04006 (2016).
[12]M. W. Tate, P. Purohit, D. Chamberlain, K. X. Nguyen, R. Hovden, C. S. Chang, P. Deb, E. Turgut, J. T. Heron, D. G. Schlom, D. C. Ralph, G. D. Fuchs, K. S. Shanks, H. T. Philipp, D. A. Muller, and S. M. Gruner, "High dynamic range pixel array detector for scanning transmission electron microscopy," Microsc. Microanal. **22**, 237–249 (2016).
[13]K. Müller-Caspary, O. Oppermann, T. Grieb, F. F. Krause, A. Rosenauer, M. Schowalter, T. Mehrtens, A. Beyer, K. Volz, and P. Potapov, "Materials characterisation by angle-resolved scanning transmission electron microscopy," Sci. Rep. **6**, 37146 (2016).
[14]A. Beyer, F. F. Krause, H. L. Robert, S. Firoozabadi, T. Grieb, P. Kükelhan, D. Heimes, M. Schowalter, K. Müller-Caspary, A. Rosenauer, and K. Volz, "Influence of plasmon excitations on atomic-resolution quantitative 4D scanning transmission electron microscopy," Sci. Rep. **10**, 17890 (2020).
[15]J. Barthel, M. Cattaneo, B. G. Mendis, S. D. Findlay, and L. J. Allen, "Angular dependence of fast-electron scattering from materials," Phys. Rev. B **101**, 184109 (2020).
[16]F. Kahl, V. Gerheim, M. Linck, H. Müller, R. Schillinger, and S. Uhlemann, "Test and characterization of a new post-column imaging energy filter," in *Advances in Imaging and Electron Physics* (Elsevier Inc., 2019), Vol. 212, pp. 35–70.
[17]R. D. Leapman, C. E. Fiori, and C. R. Swyt, "Mass thickness determination by electron energy loss for quantitative x-ray microanalysis in biology," J. Microscopy **133**, 239–253 (1984).
[18]T. Malis, S. C. Cheng, and R. F. Egerton, "EELS log –ratio technique for specimen–thickness measurement in the TEM," J. Electron Microsc. Technol. **8**, 193–200 (1988).
[19]K. Iakoubovskii, K. Mitsuishi, Y. Nakayama, and K. Furuya, "Mean free path of inelastic electron scattering in elemental solids and oxides using transmission electron microscopy: Atomic number dependent oscillatory behavior," Phys. Rev. B **77**, 104102 (2008).
[20]K. Müller, A. Rosenauer, M. Schowalter, J. Zweck, R. Fritz, and K. Volz, "Strain measurement in semiconductor heterostructures by scanning transmission electron microscopy," Microsc. Microanal. **18**, 995–1009 (2012).
[21]H. L. Robert, I. Lobato, F. Lyu, Q. Chen, S. Van Aert, D. Van Dyck, and K. Müller-Caspary, "Dynamical diffraction of high-energy electrons investigated by focal series momentum-resolved scanning transmission electron microscopy at atomic resolution," Ultramicroscopy **233**, 113425 (2022).
[22]T. Grieb, F. F. Krause, K. Müller-Caspary, S. Firoozabadi, C. Mahr, M. Schowalter, A. Beyer, O. Oppermann, K. Volz, and A. Rosenauer, "Angle-resolved STEM using an iris aperture: Scattering contributions and sources of error for the quantitative analysis in Si," Ultramicroscopy **221**, 113175 (2021).
[23]H. Kohl, "Image formation by inelastically scattered electrons: Image of a surface plasmon," Ultramicroscopy **11**, 53–65 (1983).
[24]H. Kohl and H. Rose, Adv. Electron. Electron Phys. **65**, 173–227 (1985).
[25]M. Tanaka, K. Tsuda, M. Terauchi, K. Tsuno, T. Kaneyama, T. Honda, and M. Ishida, "A new 200 kV Ω-filter electron microscope," J. Microscopy **194**, 219–227 (1999).
[26]T. Grieb, F. F. Krause, C. Mahr, D. Zillmann, K. Müller-Caspary, M. Schowalter, and A. Rosenauer, "Optimization of {NBED} simulations for disc-detection measurements," Ultramicroscopy **181**, 50–60 (2017).
[27]R. F. Egerton and K. Wong, "Some practical consequences of the Lorentzian angular distribution of inelastic scattering," Ultramicroscopy **59**, 169–180 (1995).
[28]R. F. Egerton, R. A. Mcleod, and M. Malac, "Validity of the dipole approximation in TEM-EELS studies," Microsc. Res. Tech. **77**, 773–778 (2014).
[29]J. C. Lagarias, J. A. Reeds, M. H. Wright, and P. E. Wright, "Convergence properties of the Nelder-Mead simplex method in low dimensions," SIAM J. Optim. **9**, 112–147 (1998).